



HAL
open science

Computational homogenization of a physically-based crystal plasticity law for irradiated bainitic steels

Loïc Chaix, Mihail Gă răjeu, Mart ín Idiart, Ghiath Monnet, Pierre-Guy Vincent

► **To cite this version:**

Loïc Chaix, Mihail Gă răjeu, Mart ín Idiart, Ghiath Monnet, Pierre-Guy Vincent. Computational homogenization of a physically-based crystal plasticity law for irradiated bainitic steels. Computational Materials Science, 2025, 10.1016/j.commatsci.2024.113316 . hal-04688578

HAL Id: hal-04688578

<https://hal.science/hal-04688578v1>

Submitted on 5 Sep 2024

HAL is a multi-disciplinary open access archive for the deposit and dissemination of scientific research documents, whether they are published or not. The documents may come from teaching and research institutions in France or abroad, or from public or private research centers.

L'archive ouverte pluridisciplinaire **HAL**, est destinée au dépôt et à la diffusion de documents scientifiques de niveau recherche, publiés ou non, émanant des établissements d'enseignement et de recherche français ou étrangers, des laboratoires publics ou privés.

Computational homogenization of a physically-based crystal plasticity law for irradiated bainitic steels

Loïc Chaix^{a,b}, Mihail Garajeu^{a,*}, Martín I. Idiart^{c,d}, Ghiath Monnet^e, Pierre-Guy Vincent^b

^a*Aix-Marseille Univ, CNRS, Centrale Marseille, LMA, 4 Impasse Nikola Tesla, CS 40006, 13453 Marseille Cedex 13, France.*

^b*Institut de Radioprotection et de Sûreté Nucléaire (IRSN), PSN-RES/SEMIA/LSMA, B.P. 3, 13115 Saint-Paul-lez-Durance Cedex, France.*

^c*Centro Tecnológico Aeroespacial/Departamento de Ingeniería Aeroespacial, Facultad de Ingeniería, Universidad Nacional de La Plata, Avda. 1 esq. 47 S/N, La Plata B1900TAG, Argentina.*

^d*Consejo Nacional de Investigaciones Científicas y Técnicas (CONICET), CCT La Plata, Calle 8 N° 1467, La Plata B1904CMC, Argentina.*

^e*EDF - R&D, MMC, Avenue des Renardières, Moret sur Loing, France.*

Abstract

The elasto-viscoplastic response of irradiated bainitic steels for pressure vessels of light water reactors is described by a multiscale micromechanical model. The model relies on a simplified set of complex constitutive equations describing intragranular flow under a wide range of temperatures, strain rates, and irradiation levels. These equations were themselves partially calibrated by multiscale analyses based on dislocation dynamics calculations, atomistic calculations, and experimental measurements. They include the contribution of jog drag, lattice friction, evolution of dislocation microstructures, and irradiation hardening. The scaling up of these intragranular laws to polycrystalline samples relies on a computational homogenization method which solves the field equations within periodic representative volume elements by means of Fast Fourier Transforms. This computational method proves advantageous relative to the finite element method in handling the complex microstructural morphology of the model required to achieve overall constitutive isotropy. Macroscopic simulations for uniaxial curves under different irradiation levels are first confronted to experimental curves to identify certain microscopic material parameters employed to describe the evolution of the mean-free path of dislocations with deformation. Subsequent comparisons for the evolution of the yield stress, irradiation hardening and the response to sudden strain-rate variations are then reported for a class of steels with various chemical compositions under wide ranges of temperature, loading rate and irradiation level. Good agreement is obtained in all cases. Finally, simulations are employed to explore the influence of the initial dislocation density on the intragranular stress and strain fields. An appreciable influence on the fields is observed during the elasto-viscoplastic transition but not deep in the plastic range.

Keywords: steels, neutron radiation, crystal plasticity, computational homogenization

1. Introduction

The mechanical integrity of pressure vessels is a critical issue in the long-term safety assessment of light water reactors. These vessels are made of bainitic steels which undergo progressive embrittlement with

*Corresponding author:

Email addresses: lchaix@lma.cnrs-mrs.fr (Loïc Chaix), mihai.garajeu@univ-amu.fr (Mihail Garajeu), martin.idiart@ing.unlp.edu.ar (Martín I. Idiart), ghiath.monnet@edf.fr (Ghiath Monnet), pierre-guy.vincent@irsna.fr (Pierre-Guy Vincent)

neutron radiation. Accounting for this embrittlement in advanced failure criteria requires knowledge of the entire elastoplastic response of the steels for a wide range of deformation rates, temperatures, and radiation doses [1]. Such a range of working conditions hampers the use of purely phenomenological descriptions of material behavior and calls for physically-based descriptions that explicitly account for the micromechanisms responsible for the behavior.

At the microscopic scale, bainitic steels exhibit a polycrystalline structure of a small grain size, mainly composed of ferritic laths packages and cementite inclusions [2, 3]. At smaller scales, a high density of dislocations, intragranular carbides and irradiation defects, such as solute clusters and dislocation loops, are observed [1]. Monnet et al. [4] have recently adapted the crystal plasticity law reported in [5] for pure iron to bainitic steels. The law accounts for multiple physical phenomena and follows from multi-scale analyses based on dislocation dynamics calculations, atomistic calculations, as well as on experimental observations. It considers two contributions to the intragranular plastic slip rate through a harmonic sum, each one depending on the resolved stress and on dislocation densities in a strongly nonlinear manner, and furthermore, involve critical resolved stresses which depend on the strain rate. Recent experience suggests that certain simplifications to this crystal plasticity law, such as a reduction in the number of internal variables employed, can be introduced without appreciably altering its descriptive capabilities. The first purpose of this work is to put forward such simplified law, which is spelled out in Section 2. To assess their descriptive capabilities, crystal plasticity laws must be scaled up by some homogenization procedure. The second purpose of this work is to report on the suitability of a computational homogenization method based on the Fast Fourier Transform (FFT) to scale up crystal plasticity laws. The method has recently proved successful in scaling up a subclass of this crystal plasticity law wherein one of the two contributions to the plastic slip rate dominates [6]. From its inception [7], FFT methods have been widely used for computing the overall mechanical response of heterogeneous materials with complex microstructures, see [8] for a recent review. Compared to the finite elements method [9, 10], the advantage of using a FFT method generally lies in a more rapid computation and in a complexity reduction due to the absence of the mesh and the natural way to incorporate the periodicity conditions. Lebensohn [11] used for the first time the iterative scheme proposed by Moulinec and Suquet in the context of polycrystalline materials, followed by many other works, see [12] for a recent review about computational simulations of the mechanical behavior of polycrystalline materials. It was remarked that the classical FFT scheme is less accurate in the case of low rate-sensitivity materials or in the case of composite materials with high contrast between phases [13]. To overcome this limitation, but also in order to accelerate the convergence of the iterative method, different improved FFT formulations were proposed [13, 14, 15] and compared in [16]. In the present work, the basic scheme spelled out in Section 3 is employed. Homogenized models exhibiting overall constitutive isotropy follow from representative volume elements with the required microstructural complexity. A third purpose of this work is to confront model predictions with experimental measurements on a class of bainitic steels, and thus infer certain material parameters employed by the simplified crystal plasticity law to describe the evolution of intragranular mean-free path of dislocations during deformation. Comparisons for a wide range of scenarios are reported in Section 4. In addition, the homogenized model is employed to explore the influence of initial dislocation densities on the intragranular stress and strain fields. Finally, Section 5 closes the exposition with a summary of the main conclusions.

2. A simplified crystal plasticity law for irradiated bainitic steels

Central to the multiscale model developed in this work is a simplified version of the physically-based crystal plasticity law of [4] for bainitic steels. Compared to the original version, it involves fewer equations and simpler expressions, and therefore eases numerical implementations. In the following, the upper indexes (s) refer to the slip system number, while the lower indexes refer to the nature of the variable.

The crystal law assumes an additive decomposition of the infinitesimal strain into elastic and viscoplastic parts such that

$$\dot{\boldsymbol{\epsilon}} = \mathbb{C}^{-1} : \dot{\boldsymbol{\sigma}} + \sum_{s=1}^N \dot{\gamma}^{(s)} \boldsymbol{\mu}^{(s)}, \quad (1)$$

51 or equivalently

$$\dot{\boldsymbol{\sigma}} = \mathbb{C} : \left(\dot{\boldsymbol{\varepsilon}} - \sum_{s=1}^N \dot{\gamma}^{(s)} \boldsymbol{\mu}^{(s)} \right), \quad (2)$$

52 where the symbol ":" represents the doubly contracted tensor product, $\boldsymbol{\varepsilon}$ and $\boldsymbol{\sigma}$ are the total strain and
 53 Cauchy stress tensors, respectively, while $\dot{\gamma}^{(s)}$ and $\boldsymbol{\mu}^{(s)}$ are the slip rate and Schmid tensor of system s .
 54 The elastic deformation is fully characterized by the stiffness tensor \mathbb{C} , which is assumed isotropic with
 55 shear modulus μ and Poisson's ratio ν . The viscoplastic deformation, in turn, is assumed to occur by
 56 slip along twelve slip systems ($N = 12$) belonging to the family $\langle 111 \rangle \{110\}$. In this connection, it should
 57 be remarked that the original crystal law [4] admitted slip over $\{112\}$ planes also. However, simulations
 58 suggested that the contribution of these additional slip planes to the overall deformation was not significant
 59 even for temperatures for which $\{112\}$ slip is theoretically likely to be activated.

60 2.1. Slip rates

61 The crystal law further assumes that each slip rate $\dot{\gamma}^{(s)}$ is the harmonic mean of a slip rate $\dot{\gamma}_{drag}^{(s)}$ controlled
 62 by jog-drag and a slip rate $\dot{\gamma}_{friction}^{(s)}$ controlled by lattice friction. In bainitic steels, two types of dynamic
 63 obstacles control the effective stress: the lattice friction at low temperature resulting from the non-planar
 64 core structure of screw dislocations and jog drag induced by the thermally activated motion of jogs formed
 65 by intersection of mobile screw dislocations with forest dislocations whose Burgers vector is outside the slip
 66 plane. The harmonic sum

$$\dot{\gamma}^{(s)} = \left(\frac{1}{\dot{\gamma}_{drag}^{(s)}} + \frac{1}{\dot{\gamma}_{friction}^{(s)}} \right)^{-1} \quad (3)$$

67 reflects the fact that the slip occurs according to the characteristic times of the two physical phenomena.
 68 Each slip rate is given by

$$\dot{\gamma}_{drag}^{(s)} = \dot{\gamma}_{0,drag} \sinh \left(p_{drag} \frac{\tau_{eff}^{(s)}}{\tau_c^{(s)}} \right) \text{sgn} \left(\tau^{(s)} \right) \quad (4)$$

69 and

$$\dot{\gamma}_{friction}^{(s)} = \dot{\gamma}_{0,friction} \exp \left(-\frac{\Delta G_0}{kT} \right) \sinh \left(\frac{\Delta G_0}{kT} \sqrt{\frac{\tau_{eff}^{(s)}}{\tau_0}} \right) \text{sgn} \left(\tau^{(s)} \right), \quad (5)$$

70 where k is the Boltzmann constant, T is the absolute temperature, $\tau^{(s)} = \boldsymbol{\sigma} : \boldsymbol{\mu}^{(s)}$ is the resolved shear
 71 stress, $\tau_{eff}^{(s)}$ is an effective shear stress defined below, and the remaining symbols refer to material param-
 72 eters characterizing slip. At high temperatures or low rates the flow is controlled by (4), whereas at low
 73 temperatures or high rates the flow is controlled by (5). For both regimes, a hyperbolic sine function is
 74 introduced to account for the probability, at low stress, of thermal activation in the opposite direction. This
 75 is an important improvement of the original model, since it allows to avoid discontinuity of slip rate at zero
 76 effective stress.

77 Given the common microstructural features in all bainitic steels, only the term $\tau_c^{(s)}$ varies between specific
 78 steels and increase with deformation in expressions (4) and (5). In these two equations, $\tau_{eff}^{(s)}$ is the effective
 79 shear stress for each slip system, that is, the net driving force for dislocation motion

$$\tau_{eff}^{(s)} = \max \left(|\tau^{(s)}| - \tau_c^{(s)}, 0 \right). \quad (6)$$

80 The shear stress for each slip system is split into the critical shear stress, $\tau_c^{(s)}$, representing the yield surface
 81 at the given strain rate, and the effective shear stress $\tau_{eff}^{(s)}$ necessary to force screw dislocations to move at
 82 the velocity required to accommodate the imposed strain rate.

2.2. Critical shear stresses

In bainitic steels, the flow stress is controlled by a low-alloy Fe-C solid solution, intragranular carbide particles, high density of dislocations, small grain size (large Hall-Petch effect) and, if irradiated, irradiation defects such as dislocations loops (*DLs*) and solute clusters (*SCs*). These features can be classified into two families: local obstacles (dislocations, carbides, SC, etc.) and diffuse (or long-range) obstacles inducing solid solution and the Hall-Petch effect. Since solid solution and carbide contributions to the flow stress are substantially lower than the Hall-Petch effect and forest hardening, respectively, we incorporate the contribution of solid solution into that of the Hall-Petch effect (through a slight decrease in grain size) and we incorporate the carbide contribution into that of forest dislocations (through a small increase in dislocation density). This is a second simplification of the original model [4]. Thus, the critical stress is reduced to

$$\tau_c^{(s)} = \sqrt{\left(\tau_{auto}^{(s)}\right)^2 + \left(\max\left(\tau_{forest}^{(s)} - \tau_{eff}^{(s)}, 0\right)\right)^2 + (\tau_{DL})^2 + (\tau_{SC})^2 + \tau_{HP}}, \quad (7)$$

where the components

$$\tau_{auto}^{(s)} = \mu b \sqrt{a^{(s)(s)} \rho^{(s)}} \quad \text{and} \quad \tau_{forest}^{(s)} = \mu b \sqrt{\sum_{s \neq j} a^{(s)(j)} \rho^{(j)}}$$

account for the interactions of the dislocations belonging to the same slip system and for interactions of the dislocations belonging to different slip systems, respectively, while the remaining components

$$\begin{aligned} \tau_{DL} &= \mu b \sqrt{a_{DL} d_{DL} c_{DL}}, \\ \tau_{SC} &= \mu \sqrt{p_{SC,1} (d_{SC})^{2.3} (c_{SC})^{1.14}}, \quad (d_{SC} \text{ in nm and } c_{SC} \text{ in } 10^{22} \times \text{m}^{-3}), \\ \tau_{HP} &= \frac{\mu}{\mu_{300K}} \frac{K_{HP}}{\sqrt{d}}, \end{aligned}$$

do not depend on the internal variables —and hence on the mechanical process— and refer, respectively, to the resistance of dislocation loops, solute clusters, and finally the contribution of the Hall-Petch effect —including solid solution— which depends on the average ferrite lath package size d . The internal variables $\rho^{(s)}$ refer to the dislocation densities on each active slip system. The Hall-Petch effect is here only described by a mean grain size d . It has been shown that the sizes of the ferrite lath packages and old austenitic grains are proportional [17], which justify the choice of a single parameter to describe the microstructure. The added value of our work is to show that we can isolate the Hall-Petch effect and obtain a flow stress while respecting both the experimentally measured dislocation densities and the Hall-Petch law with an experimentally measured Hall-Petch constant, which was not a foregone conclusion. In turn, the volume densities of irradiation defects c_{DL} and c_{SC} and their sizes d_{DL} and d_{SC} are material parameters that can be predicted by microstructure models or measured in experiment. The interaction coefficients $a^{(s)(j)}$ are defined such that, taking into account the results of dislocation dynamics simulations and by making a first order approximation on the strength of the junctions, two different values are considered: 0.7 for the collinear interactions (system sharing the same Burgers vector) and 0.1 for all other configurations. The remaining symbols in these expressions are defined in Table 1, unless some parameter values which are obtained by comparison with experimental data and will be given further. As pointed out in [4], an important modification to the original model is that the contributions of *DL* and *SC* are now outside the $\max()$ term in expression (7). The reason was discussed in [4]. This modification is significant and must be taken into account.

2.3. Evolution of dislocation densities

Physically-based crystal plasticity laws include equations for the evolution of the internal variables describing the microstructure (dislocations, dislocations loops, solutes clusters, among others). It is assumed that only the dislocation density on each slip system can vary (dislocation loops and solute cluster densities

Symbol	Parameter	Value	Units
μ	shear modulus	$82819.0 - 8.17 T(K)$ $-0.0213 T^2(K)$	MPa
ν	Poisson ratio	0.3	–
$\dot{\gamma}_{0,drag}$	reference slip rate for the jog drag contribution	10^{-5}	s^{-1}
$\dot{\gamma}_{0,friction}$	reference slip rate for the lattice friction contribution	10^9	s^{-1}
p_{drag}	parameter adjusted from experimental results	200.0	–
ΔG_0	parameter adjusted from experimental results	0.84	eV
k	Boltzmann constant	8.6×10^{-5}	$eV.K^{-1}$
τ_0	reference critical shear stress	300.0	MPa
K_{HP}	constant related to the Hall-Petch effect	0.28	$MPa.m^{1/2}$
b	Burger vector norm	0.248	nm
a_{DL}	interaction coefficient for dislocation loops	0.25	–
$p_{SC,1}$	parameter related to the solute clusters	$0.3722 \times 10^{-12.38}$	$m^{1.12}$
p_d	parameter related to the ferrite lath package size	3.455	–
$p_{SC,2}$	parameter related to the solute clusters	4.0775×10^{11}	$m^{-5/4}$
T_0	characteristic temperature	217.4	K
$\rho_{init}^{(s)}$	initial dislocation density on each slip system	*	m^{-2}
d	average ferrite lath package size	*	μm
K_{auto}	number of obstacles (dislocation of the same system)	*	–
K_{forest}	number of obstacles (dislocation of a different system)	*	–
K_{DL}	number of obstacles (dislocation loops)	*	–
K_{SC}	number of obstacles (solute clusters)	*	–
p_y	parameter related to the annihilation distance	*	nm
d_{DL}	characteristic diameter of dislocation loops	*	nm
c_{DL}	concentration of dislocation loops	*	m^{-3}
d_{SC}	characteristic diameter of solute clusters	*	nm
c_{SC}	concentration of solute clusters	*	m^{-3}

Table 1: Material parameters of the crystal plasticity law. Numerical values correspond to steels resembling A508 cl.3 RPV available from the literature. Starred values are determined in this work.

120 remain fixed). According to the Kocks-Mecking classical theory [18], the storage of dislocations results
121 from their immobilization after sliding over a distance λ , called mean free path. On the other hand, when
122 the density increases sharply, spacing between dislocations decreases strongly. Below a critical spacing y
123 (the annihilation distance), it is assumed that dipoles are no longer stable and annihilate spontaneously by
124 thermal activation. The classical Kocks-Mecking formulation [18] can be written as

$$\dot{\rho}^{(s)} = \frac{|\dot{\gamma}^{(s)}|}{b} \left(\frac{1}{\lambda^{(s)}} - y\rho^{(s)} \right) \quad (8)$$

125 with the total mean free path of dislocations

$$\frac{1}{\lambda^{(s)}} = \frac{p_d}{d} + \frac{\sqrt{a^{(s)(s)}\rho^{(s)}}}{K_{auto}} + \frac{\sqrt{\sum_{s \neq j} a^{(s)(j)}\rho^{(j)}}}{K_{forest}} + \frac{\left(\frac{c_{SC}}{p_{SC,2}}\right)^{4/7}}{K_{SC}} + \frac{\sqrt{a_{DL} d_{DL} c_{DL}}}{K_{DL}}. \quad (9)$$

126 Each term in this last expression corresponds to a different class of obstacles to dislocation movement. The
 127 constants K_i represent the number of obstacles of the family i that can be overcome by a dislocation before
 128 its immobilization. In other words, equation (9) means that a dislocation is immobilized when it reaches
 129 a grain boundary and each time it encounters K_i obstacles of the family i . The values for the parameters
 130 K_i therefore influence hardening. A notable consequence of this approach is the presence of irradiation
 131 defects which modify the rate of the hardening in the irradiated materials. Due to thermal activation, the
 132 annihilation distance y depends on temperature according to

$$y = p_y \min(1, 0.255 e^{T/T_0}). \quad (10)$$

133 The remaining material parameters entering expressions (2) to (10) are described in table 1. The numerical
 134 values reported in that table correspond to steels resembling A508 cl.3 RPV steels of interest in this work.
 135 The starred values will be chosen later for specific steels and determined from comparisons with experimental
 136 uniaxial curves.

137 3. Computational homogenization method

138 The macroscopic behavior of polycrystalline aggregates is characterized by the relation between the
 139 volume averages over the representative volume element of the local stress field, denoted $\bar{\boldsymbol{\sigma}}(t)$, and the local
 140 strain field, denoted $\bar{\boldsymbol{\varepsilon}}(t)$, where t is the time. To compute the stress and strain fields for a given loading
 141 condition, the constitutive equations presented in Section 2 are implemented in the computer code CraFT [19]
 142 which solves the mechanical field equations by means of a Fast Fourier Transform (FFT) based algorithm
 143 proposed in [20], [7], and [21] to determine the effective properties of periodic composites with complex
 144 microstructures. As in studies [22] and [23] devoted to the effective behavior of porous viscoplastic crystals
 145 and polycrystals, the so-called "basic" iterative scheme is adopted, which ensures the strain compatibility.
 146 At each time step CraFT determines the local stress and strain fields $(\boldsymbol{\sigma}, \boldsymbol{\varepsilon})$ by a fixed point algorithm

$$\begin{cases} \boldsymbol{\varepsilon}^{i+1} = \boldsymbol{\varepsilon}^i - \boldsymbol{\Gamma}^0 * \boldsymbol{\sigma}^i \\ \boldsymbol{\sigma}^{i+1} = \mathcal{F}(\boldsymbol{\varepsilon}^{i+1}, \boldsymbol{\varepsilon}^i, \mathbf{v}_{int}) \end{cases} \quad (11)$$

147 where at each iteration step i of the iterative scheme, the system of constitutive equations of the model,
 148 giving the function \mathcal{F} , is integrated in time using a fully implicit scheme (\mathbf{v}_{int} corresponds to the internal
 149 variables). In (11) the operator $\boldsymbol{\Gamma}^0$ is the Green operator associated to an elasticity tensor \mathbb{C}_0 of an infinite
 150 medium (* denotes the convolution operator). The choice of \mathbb{C}_0 can depend on the local constitutive behavior
 151 being simulated and plays an important role in the convergence rate of the algorithm. The present work
 152 relies on the choice already implemented in the code CraFT.

153 3.1. Convergence criteria

154 Since the "basic" scheme used in the computations presented in this work ensures the compatibility of
 155 the strain, only two convergence criteria are checked, one for the equilibrium condition and the other for the
 156 macroscopic stress direction (see Figure 1 of [24] for an intuitive representation of the convergence path).
 157 At each iteration i of the general algorithm in CraFT, the error relative to the local equilibrium condition
 158 is given by

$$\frac{\sqrt{\langle \|\text{div}(\boldsymbol{\sigma}^i)\|^2 \rangle}}{\|\langle \boldsymbol{\sigma}^i \rangle\|} \quad (12)$$

Algorithm inputs: $\dot{\boldsymbol{\epsilon}}^n$, $\boldsymbol{\sigma}^{n-1}$, $\dot{\gamma}^{n-1}$, τ_c^{n-1} and ρ^{n-1}

1 Initialization of the stress and the internal variables

$$\boldsymbol{\sigma}^{n,0} = \boldsymbol{\sigma}^{n-1}, \dot{\gamma}^{n,0} = \dot{\gamma}^{n-1}, \tau_c^{n,0} = \tau_c^{n-1} \text{ and } \rho^{n,0} = \rho^{n-1}$$

2 Initialization of the error $\epsilon = tol + 1$

3 While $\epsilon > tol$

3.1 Calculation of $\boldsymbol{\sigma}^{n,i}$, $\dot{\gamma}^{n,i}$, $\tau_c^{n,i}$ and $\rho^{n,i}$

$$\boldsymbol{\sigma}^{n,i} = \boldsymbol{\sigma}^{n-1} + \Delta t f_1(\dot{\gamma}^{n,i-1}, \dot{\boldsymbol{\epsilon}}^n), f_1 \text{ corresponds to (2)}$$

$$\dot{\gamma}^{n,i} = f_2(\tau_c^{n,i-1}, \boldsymbol{\sigma}^{n,i-1}), f_2 \text{ corresponds to (3)}$$

$$\tau_c^{n,i} = f_3(\tau_c^{n,i-1}, \rho^{n,i-1}, \boldsymbol{\sigma}^{n,i-1}), f_3 \text{ corresponds to (7)}$$

$$\rho^{n,i} = \rho^{n-1} + \Delta t f_4(\rho^{n,i-1}, \dot{\gamma}^{n,i-1}), f_4 \text{ corresponds to (8)}$$

3.2 Calculation of the error

$$\epsilon_\sigma = 2 \|\boldsymbol{\sigma}^{n,i} - \boldsymbol{\sigma}^{n,i-1}\| / \|\boldsymbol{\sigma}^{n,i} + \boldsymbol{\sigma}^{n,i-1}\|$$

$$\epsilon_\gamma = 2 \|\dot{\gamma}^{n,i} - \dot{\gamma}^{n,i-1}\| / \|\dot{\gamma}^{n,i} + \dot{\gamma}^{n,i-1}\|$$

$$\epsilon_{\tau_c} = 2 \|\tau_c^{n,i} - \tau_c^{n,i-1}\| / \|\tau_c^{n,i} + \tau_c^{n,i-1}\|$$

$$\epsilon_\rho = 2 \|\rho^{n,i} - \rho^{n,i-1}\| / \|\rho^{n,i} + \rho^{n,i-1}\|$$

$$\epsilon = \max(\epsilon_\sigma, \epsilon_\gamma, \epsilon_{\tau_c}, \epsilon_\rho)$$

3.3 Updating variables, affected by a weight $w \in [0, 1]$ (in order to facilitate the convergence)

$$\boldsymbol{\sigma}^{n,i} = w \boldsymbol{\sigma}^{n,i-1} + (1 - w) \boldsymbol{\sigma}^{n,i}$$

$$\dot{\gamma}^{n,i} = w \dot{\gamma}^{n,i-1} + (1 - w) \dot{\gamma}^{n,i}$$

$$\tau_c^{n,i} = w \tau_c^{n,i-1} + (1 - w) \tau_c^{n,i}$$

$$\rho^{n,i} = w \rho^{n,i-1} + (1 - w) \rho^{n,i}$$

Algorithm output: $\boldsymbol{\sigma}^n$

Table 2: Algorithm used for the numerical integration of the local crystal plasticity law in CraFT

159 where $\langle \boldsymbol{\sigma}^i \rangle$ denotes the volume average of the field $\boldsymbol{\sigma}^i$ and $\|\cdot\|$ denotes the Frobenius norms of a vector or
 160 a second-order tensor. This error is computed in the Fourier space. The error relative to the prescribed
 161 direction of the macroscopic stress is defined by

$$\frac{\|\langle \boldsymbol{\sigma}^i \rangle - \boldsymbol{\Sigma}_0 k^i\|}{\|\boldsymbol{\Sigma}_0 k^i\|}. \quad (13)$$

162 where $\boldsymbol{\Sigma}_0$ is the direction of the macroscopic stress and k^i indicates the level of macroscopic stress. In
 163 this work, the tolerances for both criteria are set to 10^{-3} (see also the general presentation of the two
 164 corresponding convergence tests in [25]).

165 3.2. Time integration of the local crystal plasticity law

166 The set of equations associated with the crystal plasticity law is highly nonlinear. A fully implicit scheme
 167 is chosen (implicit Euler scheme resolved by a fixed point algorithm) in order to determine the stress $\boldsymbol{\sigma}^{i+1}$
 168 for a given strain $\boldsymbol{\epsilon}^{i+1}$, at each CraFT iteration. The numerical procedure is presented in Table 2. In this

	C	S	P	Si	Cr	Mo	Mn	Ni	V	Al	Co	Cu
A	0.139	0.004	0.006	0.19	0.21	0.49	1.33	0.73	< 0.01	0.025	0.020	0.06
B	0.160	0.004	0.008	0.22	0.22	0.51	1.33	0.76	< 0.01	/	0.017	0.07
C	0.140	/	0.005	0.23	/	0.55	1.44	0.86	/	/	/	0.41
D	0.150	0.006	0.013	0.22	0.19	0.52	1.31	0.70	0.009	0.022	0.020	0.07

Table 3: Chemical composition in weight % of the various steels considered in this study

169 table, the index n and $n - 1$ respectively refer to the current and previous times (Δt is the time step) and
170 the index i and $i - 1$ respectively refer to the current and previous iteration of the fixed point algorithm.

171 4. Results and discussion

172 The predictive capabilities of the homogenized model are assessed by confronting predictions with ex-
173 perimental uniaxial curves of four bainitic steels of a common class. Each steel is identified with letters A
174 through D for ease of presentation; their chemical compositions are displayed in Table 3. Types A and D
175 refer to a low copper steel and a 16MND5 steel, both resembling an A508 cl.3 steel. Type B refers to a
176 16MND5 steel employed in vessels for pressurized water reactors and manufactured by Framatome; it was
177 subject to two austenitizing treatments followed by water quenching and tempering, and a final stress relief
178 treatment to obtain a tempered bainitic microstructure. Finally, type C refers to RPV steel. For these
179 steels, it is reasonable to assume that the influence of dislocation loops is negligible compared to that of
180 solute clusters. Therefore, we set $c_{DL} = 0$ henceforth, and ignore the irrelevant parameters K_{DL} and d_{DL} .
181 The reminder of the unquantified material parameters of Table 1 are identified by comparisons of predictions
182 with experiments. To that end, uniaxial curves are simulated by applying mixed loading conditions of the
183 form

$$\bar{\sigma}(t) = k(t)\Sigma_0 \quad \text{and} \quad \Sigma_0 : \dot{\bar{\epsilon}} = \dot{E}, \quad (14)$$

184 where $k(t)$ is an unknown scalar function, evolving in time, $\bar{\epsilon}$ and $\bar{\sigma}$ are the macroscopic strain and stress,
185 $E(t) = \dot{E} t$ is the prescribed projected macroscopic strain in the Σ_0 direction. We begin by identifying a
186 suitable microstructural morphology for the computational model such that the simulated uniaxial curve
187 produced by (14) is insensitive to loading direction Σ_0 . In the following, the tolerance tol is set to 10^{-4} and
188 the weight w is set to 0.9.

189 4.1. Microstructural morphology

190 The microstructural morphology of bainitic steels is idealized as a periodic aggregate of grains defining a
191 Voronoi tessellation. Note that the FFT method can also be used to perform computations on other types
192 of tessellations, such as those of Johnson-Mehl-Avrami-Kolmogorov and Laguerre, see [26]. A Voronoi tes-
193 sellation is generated from random grain seeds using a minimal distance algorithm. Crystalline orientations
194 within grains are randomly generated from a Sobol sequence (e.g. [27]) in order to approach an isotropic
195 polycrystal while optimizing the number of grains. The number of grains and voxels taken for the unit cell
196 follows from the two parametric studies in order to determine the "optimal" configuration, with a good
197 compromise between the computation time and the representativeness of the polycrystal. Simulations are
198 performed on unirradiated specimens at a temperature of 25°C and a constant strain rate of $\dot{E} = 5 \times 10^{-4} s^{-1}$.
199 The following parameters are considered, $\rho_{init}^{(s)} = 4.5 \times 10^{12} m^{-2}$, $d = 7.6 \mu m$, $K_{auto} = 72$, $K_{forest} = 24$ and
200 $p_y = 2.6 nm$.

201 First, a convergence study for the spatial discretization is carried out. A polycrystal with 125 grains is
202 considered. A total of seven spatial discretizations (in voxels per grain) are tested: 2^3 , 4^3 , 6^3 , 8^3 , 10^3 , 12^3
203 and 14^3 . For each discretization level, ten microgeometries for the Voronoi tessellation are generated. The
204 stabilization of the macroscopic response is evaluated with respect to the highest resolution (considered as

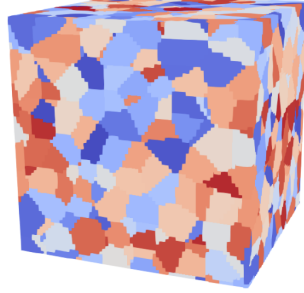


Figure 1: Unit cell with 729 grains and 373,248 voxels employed in the numerical simulations.

205 a reference and denoted hereafter k_{14^3}) by two relative errors, corresponding to the Hölder mean of order
 206 1 and infinity, respectively. For defining these two errors a discretization of the time interval is considered,
 207 $0s = t_1 < t_2 < \dots < t_N = 200s$ and the two relative errors are defined by

$$\delta_1 = \frac{1}{N} \sum_{p=1}^N \frac{|k_{14^3}(t_p) - k_\alpha(t_p)|}{|k_{14^3}(t_p)|} \quad \text{and} \quad \delta_\infty = \max_p \left\{ \frac{|k_{14^3}(t_p) - k_\alpha(t_p)|}{|k_{14^3}(t_p)|} \right\}, \quad (15)$$

208 where the index α refers to the spatial discretization. Figure 2 displays the values of these two errors with
 209 respect to the ten microgeometries considered for each discretization. Through these results, it appears
 210 that a good compromise between size and precision is obtained for 8^3 or 512 voxels per grain. From this
 211 discretization, low values of the two relative errors are observed, as well as a low dispersion of results. This
 212 discretization is retained in what follows. Taking as reference the results for the highest resolution (14^3
 213 voxels per grain) does not allow to characterize how close the results obtained for 512 voxels per grain are
 214 from the exact solution of the problem. A recent convergence result [28] shows that for linear heterogeneous
 215 materials the effective moduli obtained by the basic scheme converge to the theoretical effective moduli
 216 (as defined by the linear homogenization theory) when the resolution tends to infinity. To the best of our
 217 knowledge, there is no similar result for nonlinear materials, but it is reasonable to suppose that a higher
 218 resolution allows to better approximate the exact solution of the problem.

219 Second, the number of grains of the RVE plays a role in the macroscopic isotropy of the polycrystal.
 220 A study was carried out in order to characterize the isotropy of the polycrystal through its response to
 221 simple tensile type loadings in three different orthogonal directions. Nine numbers of grains in the RVE are
 222 considered: 2^3 , 3^3 , 4^3 , 5^3 , 6^3 , 7^3 , 8^3 , 9^3 and 10^3 and for each, five microgeometries are used. As for the
 223 previous study, the mechanical response for each tensile direction is characterized by the stress level $k(t)$
 224 versus time t . The deviation from the macroscopic isotropy is evaluated by two values, corresponding to the
 225 Hölder mean of order 1 and infinity and defined as

$$\Delta_1 = \frac{1}{N} \sum_{p=1}^N \frac{|k_{max}(t_p) - k_{min}(t_p)|}{|k_{avg}(t_p)|} \quad \text{and} \quad \Delta_\infty = \max_p \left\{ \frac{|k_{max}(t_p) - k_{min}(t_p)|}{|k_{avg}(t_p)|} \right\}, \quad (16)$$

226 where $k_{max}(t_p) = \max \{k_{[100]}(t_p), k_{[010]}(t_p), k_{[001]}(t_p)\}$, $k_{min}(t_p) = \min \{k_{[100]}(t_p), k_{[010]}(t_p), k_{[001]}(t_p)\}$,
 227 and $k_{avg}(t_p) = \frac{1}{3} (k_{[100]}(t_p) + k_{[010]}(t_p) + k_{[001]}(t_p))$. The subscript [100], [010] or [001] refers to the loading
 228 direction. Figure 3 displays the value of Δ_1 and Δ_∞ over the five microgeometries, for each number of
 229 grains. The isotropy of the polycrystal seems rather well respected from $9^3 = 729$ grains, with values of Δ_1
 230 and Δ_∞ less than 1% and a low dispersion of results.

231 In conclusion, a satisfactory unit cell results with 729 grains, each of which is discretized by about 512
 232 voxels. The cell is shown in Figure 1. With this cell, smooth convergence of the algorithm is observed.

233 4.2. Macroscopic response

234 A collection of uniaxial curves for specimens of steel type A under various conditions was generated
 235 with the homogenized model to infer the material parameters K_{auto} , K_{forest} , K_{SC} and p_y characterizing
 236 the evolution of the intragranular mean-free path of dislocations with deformation. Specifically, we consider
 237 unirradiated and irradiated specimens deforming at four different temperature levels (-100°C , -60°C ,
 238 25°C or 28°C , 200°C). Irradiated specimens were subject to intermediate ($3.6 \times 10^{23} \text{ n.m}^{-2}$) and high ($7.5 \times$
 239 10^{23} n.m^{-2}) fluences typical of RPV steels in pressurized water reactors. In all cases, the microstructural
 240 parameters $\rho_{init}^{(s)} = 4.5 \times 10^{12} \text{ m}^{-2}$ and $d = 7.6 \mu\text{m}$ are adopted. In the case of irradiated specimens, the
 241 irradiation parameters $d_{SC} = 3 \text{ nm}$ and $c_{SC} = 20.3/31.5 \times 10^{22} \text{ m}^{-3}$ for the intermediate/high fluence are
 242 adopted. Several collections of curves were obtained by sweeping the material parameters K_{auto} , K_{forest} ,
 243 K_{SC} and p_y across expected ranges of values. Figure 4 shows comparisons between the experimental curves
 244 of [1] and the predictions for a constant strain rate $\dot{E} = 5 \times 10^{-4} \text{ s}^{-1}$ obtained with the parameters reported
 245 in Table 4. The main observation in the context of this figure is that good agreement is obtained for
 246 all twelve scenarios. Indeed, the homogenized model is seen to accurately reproduce both the elastic and
 247 viscoplastic regimes at all temperatures and irradiation conditions considered. By contrast, the model is
 248 seen to miss entirely the peak stress upon yielding observed in the experimental curves. In this connection,
 249 it is recalled that peak stresses in steels have been attributed to the unpinning of Cottrell atmospheres of
 250 dislocations, which is known as static ageing. Thus, values of peak stresses tend to be highly sensitive to the
 251 thermomechanical history of the specimen and therefore show strong variability. This is one of the reasons
 252 why engineering models usually omit their description. A second reason for omitting their description is that
 253 the subsequent softening can induce localized deformations and therefore result in mesh-dependent structural

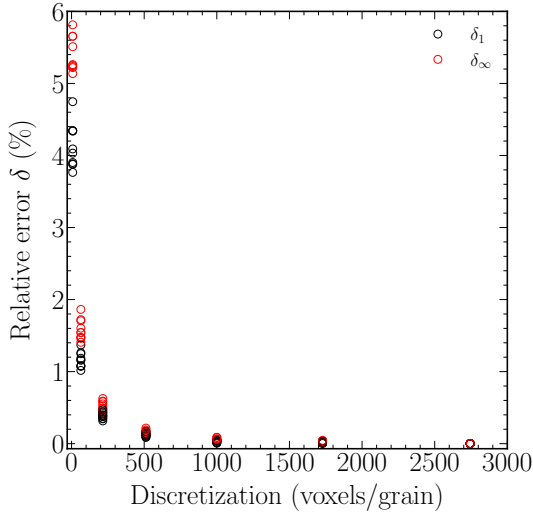


Figure 2: Relative errors with respect to the highest resolution versus voxels per grain

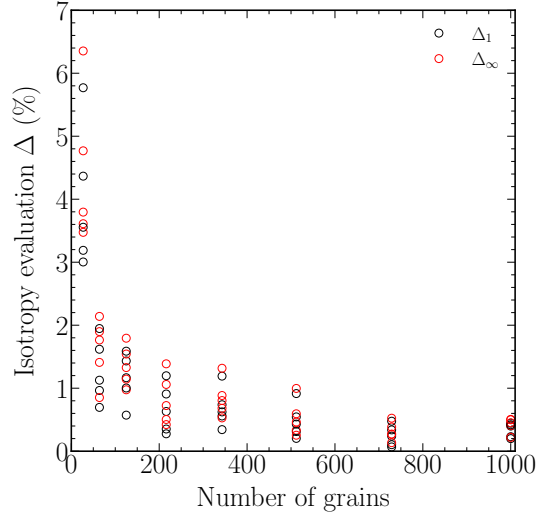


Figure 3: Quantitative estimates for the gap to the macroscopic isotropy versus the number of grains

	$\rho_{init}^{(s)} \text{ (m}^{-2}\text{)}$	$d \text{ (\mu m)}$	K_{auto}	K_{forest}	K_{SC}	$p_y \text{ (nm)}$
A	4.5×10^{12}	7.6	72	24	30	2.6
B	3.5×10^{12}	5.25	72	24	30	2.6
C	3.7×10^{12}	7.6	72	24	30	2.6
D	4.5×10^{12}	7.6	72	24	30	2.6

Table 4: Parameters identified for the various types of steel considered in this study

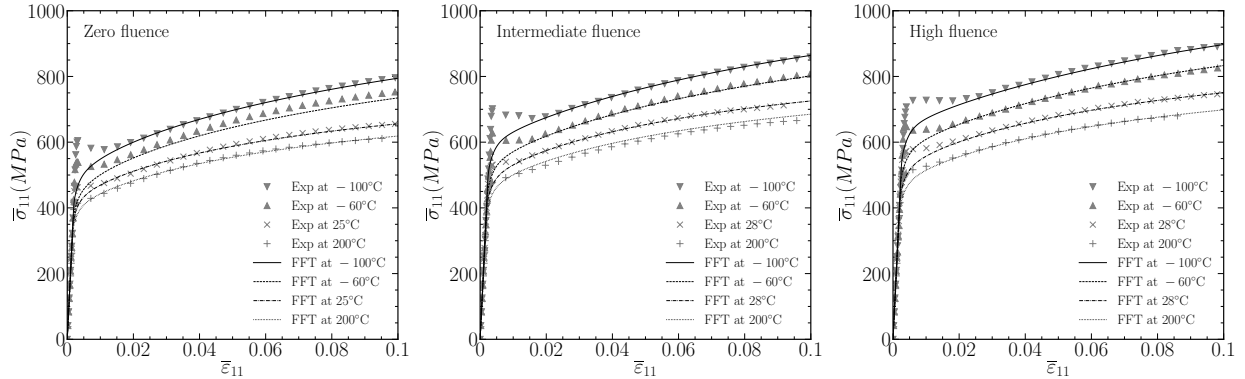


Figure 4: Comparison between experimental data and numerical simulations results of the macroscopic response of a polycrystal, under simple traction loading, for three levels of fluence : non-irradiated steel (left), intermediate fluence (center), high fluence (right)

254 simulations. Interestingly, recent multiscale simulations coupling the dynamics of irradiation defects and
 255 dislocation assembles at different spatial and temporal scales in steels suggest that, while present in the post-
 256 irradiated mechanical response, peak stresses may be absent from the mechanical response during irradiation
 257 [29]. In any event, the model can be employed to generate predictions for the evolution of a yield stress with
 258 temperature and strain rate by following common practice and defining the yield stress as the stress defined
 259 by the intercept between the tangent of the tensile curve at a deformation of 0.02 and the straight line
 260 representing the elastic part of the curve. Experimental values for a yield stress so defined in unirradiated
 261 steel specimens of type B at different strain rates have been reported in [30] (experimental values obtained
 262 from quasi-static tensile tests as well as dynamic tests using Hopkinson split bars). The values are plotted in
 263 Figure 5 versus temperature. Model predictions were generated with the parameters specified in Table 4 and
 264 imposed strain rates $\dot{E}_1 = 4.0 \times 10^{-4} \text{ s}^{-1}$, $\dot{E}_2 = 17.6 \text{ s}^{-1}$ and $\dot{E}_3 = 4000 \text{ s}^{-1}$. A very good agreement between
 265 experimental and numerical results is observed for the low and moderate strain rates, and fair agreement is
 266 observed for the highest strain rate. Thus, the model successfully captures the nonlinear decrease of yield
 267 stress with temperature at the lower strain rates. Similarly, experimental results reported in [31] for steel
 268 specimens of type C can be employed to assess the capabilities of the model to describe the influence of
 269 irradiation on hardening. Corresponding simulations are performed with the material parameters of Table 4
 270 at $T = 25^\circ\text{C}$, $\dot{E} = 5 \times 10^{-4} \text{ s}^{-1}$, and three different irradiation fluxes (3×10^{15} , 8×10^{15} , $1 \times 10^{18} \text{ n.m}^{-2}.\text{s}^{-1}$).
 271 To each flux correspond certain values of concentration and size of solute clusters. The values employed
 272 in the simulations are those experimental values reported in [31] and reproduced in Table 5. Experimental
 273 and simulated results for the magnitude $\Delta R_{p0.2} = \bar{\sigma}_{11}^{irr} - \bar{\sigma}_{11}^{unirr} \Big|_{\bar{\epsilon}_{11}^{vp}=0.002}$ are compared in Figure 6. An
 274 excellent correlation in all cases is observed. Finally, the concurrent influence of temperature and strain rate
 275 on the macroscopic response can be investigated by imposing sudden strain rate variations and measuring the
 276 induced stress jumps. Experimental measurements on steel specimens of type D have been reported in [32].
 277 Corresponding simulations are generated with the material parameters of Table 4 by considering two pairs of
 278 strain rate variations ($5 \times 10^{-4} \text{ s}^{-1} - 5 \times 10^{-3} \text{ s}^{-1}$) and ($5 \times 10^{-5} \text{ s}^{-1} - 5.0 \times 10^{-4} \text{ s}^{-1}$), for five temperatures
 279 spanning the range -100°C to 100°C , and two fluences (non-irradiated and $10 \times 10^{23} \text{ n.m}^{-2}$). This steel
 280 was subjected to irradiation in the Material Testing Reactor OSIRIS (CEA). Accelerating irradiation results
 281 from a flux which is approximately forty times higher than the flux seen by a RPV in a French pressurized
 282 water reactor [32]. At this irradiation levels the solute cluster size and concentration are $d_{SC} = 3 \text{ nm}$ and
 283 $c_{SC} = 35.1 \times 10^{22} \text{ m}^{-3}$, respectively. The simulated macroscopic tensile curves are reported in Figures 7
 284 and 8. Two series of jumps are performed for each pair of strain rates. At 2% of viscoplastic deformation,
 285 a positive strain rate jump is imposed and the strain rate value is maintained until 4% of viscoplastic
 286 deformation, followed by a negative strain rate jump, with the same amplitude. The same procedure is
 287 repeated between 6% and 8% of viscoplastic strain. In order to investigate the effect of the history of the
 288 strain rate on the macroscopic response, the low value of the pair ($5 \times 10^{-4} \text{ s}^{-1} - 5 \times 10^{-3} \text{ s}^{-1}$) and the

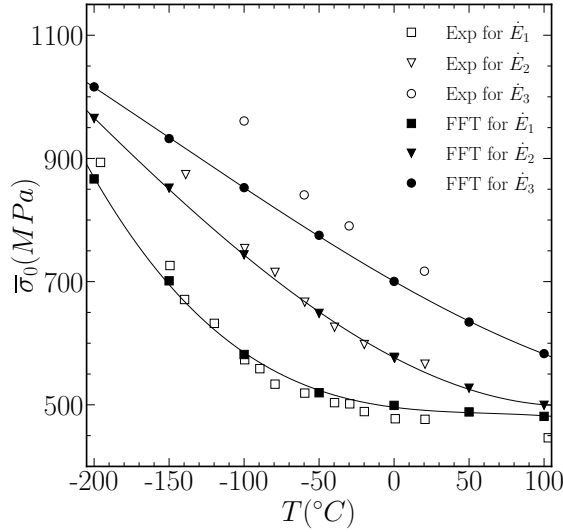


Figure 5: Evolution of the yield stress according to the temperature and the strain rate (each solid line corresponds to a quadratic fit of the FFT results)

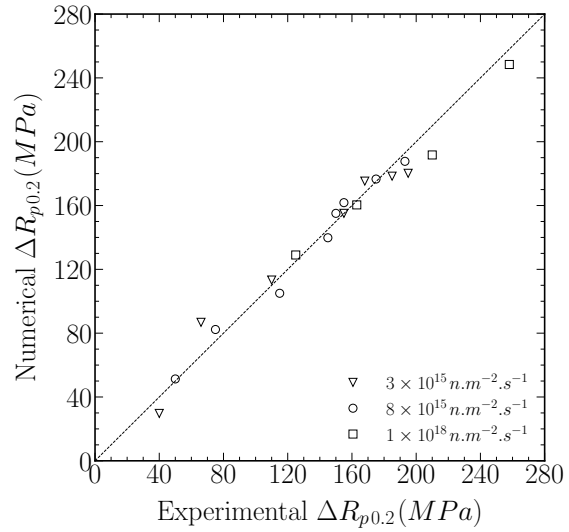


Figure 6: Comparison between experimental and numerical irradiation hardening for a total of 19 fluences through 3 fluxes

289 high value of the pair ($5 \times 10^{-5} s^{-1} - 5.0 \times 10^{-4} s^{-1}$) has been chosen equal. The simulated tensile curves
 290 reported in Figures 7 and 8 show that the behaviors of both unirradiated and irradiated specimens are
 291 almost insensitive to the strain rate history. Moreover, the strain-hardening rate (slope of the stress-strain
 292 curve) right after the jump is the same as the strain-hardening rate observed before the jump. The flow
 293 stress increases with strain rate, but the amplitude of the induced stress jumps decreases with temperature,
 294 to the extent that at $T = 100^\circ\text{C}$, for the unirradiated material, the jump is about 0.2% of the flow stress,
 295 and for the irradiated material this ratio is almost twice. The stress jump, simply defined as an absolute
 296 difference of two stress values, is then recorded for each curve of Figures 7 and 8 and is compared with
 297 the experimental results of [32]. Figures 9 and 10 show the numerical and experimental stress jumps as a
 298 function of the temperature, according to the considered fluence. A good agreement is observed between the
 299 experimentally measured jumps and those predicted by the simulations, over the entire range of temperature
 300 considered, whether for the non-irradiated or the irradiated 16MND5 steel.

301 It is concluded that the model conected in this work with a simplified crystal plasticity law and a
 302 computational homogenization method based on Fast Fourier Transforms has the capability to accurately
 303 describe the response of irradiated bainitic steels under a wide range of temperatures, irradiation levels and
 304 strain rates.

305 4.3. Effects of the initial dislocation densities

306 In almost all simulations of crystalline aggregates reported in the litterature, the initial values of the
 307 material parameters (in our case the dislocation density and grain size) are taken identically for all integration
 308 points. However, several microstructure investigations have confirmed that dislocation distribution is quite
 309 heterogenous [33]. For the first time, to the knowledge of the authors, we study the influence of the
 310 heterogeneity of dislocation distribution of the local fields and macroscopic response in an unirradiated
 311 RPV steels. Numerical simulations are carried out considering a polycrystal composed of 216 grains and
 312 discretized by 125^3 voxels. This discretization value is adopted by a convergence study carried out on
 313 the average value per phase of the Von Mises equivalent viscoplastic strain, where different resolutions are
 314 considered from 25^3 to 250^3 voxels. The imposed loading corresponds to a simple traction in the direction
 315 $[1, 0, 0]$ for a strain rate equal to $5 \times 10^{-4} s^{-1}$ and for a temperature of 25°C . The following parameters are
 316 fixed in this study $\rho_{init}^{(s)} = 4.5 \times 10^{12} m^{-2}$, $d = 7.6 \mu\text{m}$, $K_{auto} = 72$, $K_{forest} = 24$ and $p_y = 2.6 \text{ nm}$. The
 317 convergence with respect to the resolution is evaluated by comparison with the highest considered resolution

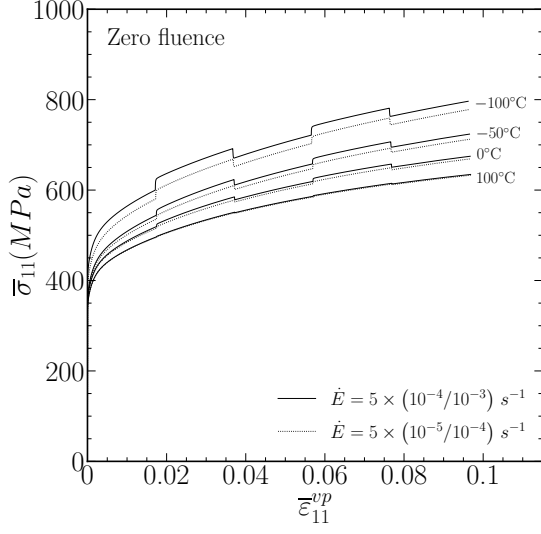


Figure 7: Simple tension behavior with abrupt strain rate variations for a non-irradiated 16MND5 steel

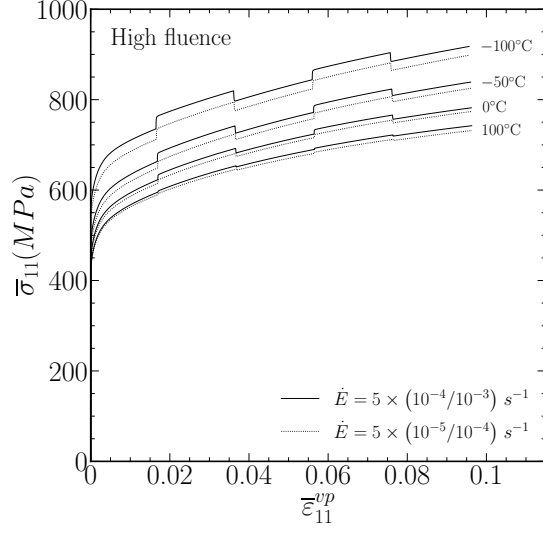


Figure 8: Simple traction behavior with abrupt strain rate variations for an irradiated 16MND5 steel

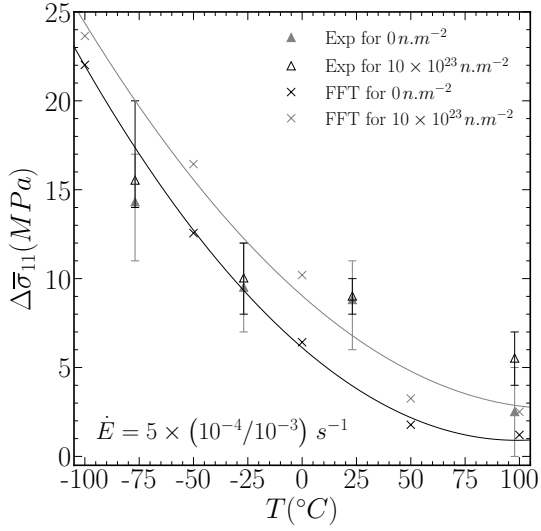


Figure 9: Stress jump as a function of the temperature for $5 \times 10^{-4} s^{-1} / 5 \times 10^{-3} s^{-1}$ strain rate variation (each solid line corresponds to a quadratic fit of the FFT results)

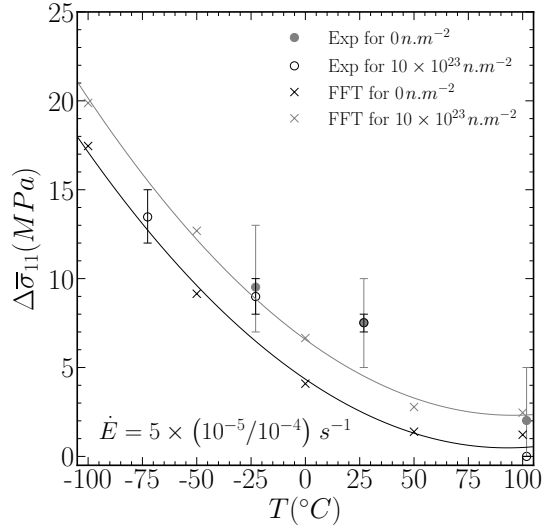


Figure 10: Stress jump as a function of the temperature for $5 \times 10^{-5} s^{-1} / 5 \times 10^{-4} s^{-1}$ strain rate variation (each solid line corresponds to a quadratic fit of the FFT results)

318 by a relative error δ , corresponding to the Hölder mean of order 1, as previously. The relative error in each
 319 phase is defined by

$$\delta = \frac{\left| \left(\frac{\overline{\varepsilon_{vp}^{eq}(r)}}{\varepsilon_{vp}^{eq}(r)} \right)_{250} - \left(\frac{\overline{\varepsilon_{vp}^{eq}(r)}}{\varepsilon_{vp}^{eq}(r)} \right)_{\alpha} \right|}{\left| \left(\frac{\overline{\varepsilon_{vp}^{eq}(r)}}{\varepsilon_{vp}^{eq}(r)} \right)_{250} \right|} \quad (17)$$

320 where r refers to the phase, $\overline{\varepsilon_{vp}^{eq}(r)}$ denotes the average value per phase of the Von Mises equivalent viscoplastic
 321 strain ε_{vp}^{eq} and α refers to the considered resolution. The results are presented in Figure 11 for a viscoplastic

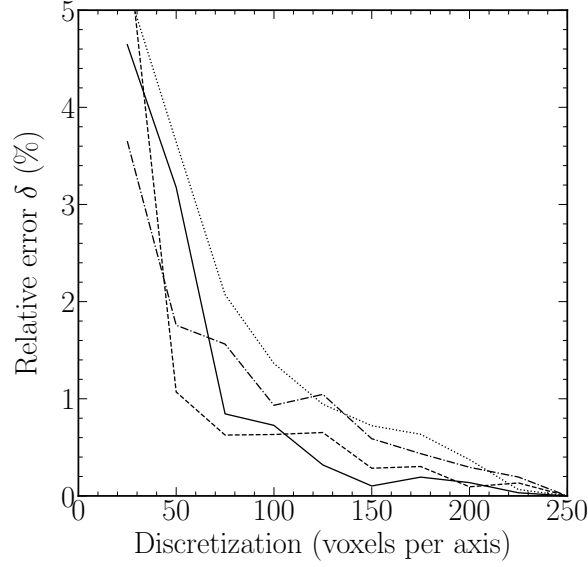


Figure 11: Relative errors with respect to the highest resolution versus total number of voxels

322 strain field obtained at 0.004 of total macroscopic strain in the tensile direction and for 4 different phases
 323 corresponding to the slowest convergence. Finally, a discretization of 125^3 voxels is chosen, corresponding
 324 to a relative error δ less than 1% and allowing then a good compromise between precision and calculation
 325 time.

326 In this study, the initial dislocation densities consists in a field defined over the polycrystal domain. Three
 327 distributions of the initial dislocation densities are considered:

- 328 1. an uniform distribution, where the initial dislocation densities are constant (equal to $\rho_{init}^{(s)}$) in the
 329 whole polycrystal,
- 330 2. a homogeneous per phase distribution, where the initial dislocation densities are uniform in each phase,

flux ($n.m^{-2}.s^{-1}$)	d_{SC} (nm)	c_{SC} ($10^{22} m^{-3}$)	exp hard (MPa)	flux ($n.m^{-2}.s^{-1}$)	d_{SC} (nm)	c_{SC} ($10^{22} m^{-3}$)	exp hard (MPa)
8×10^{15}	2.0	16.72	50.0	3×10^{15}	2.5	25.68	110.0
8×10^{15}	2.4	19.35	75.0	3×10^{15}	2.7	32.04	155.0
8×10^{15}	2.6	21.74	115.0	3×10^{15}	2.85	33.43	168.0
8×10^{15}	2.6	30.44	145.0	3×10^{15}	3.1	28.86	185.0
8×10^{15}	2.7	32.04	150.0	3×10^{15}	3.2	27.41	195.0
8×10^{15}	2.8	31.34	155.0	1×10^{18}	2.15	40.38	125.0
8×10^{15}	2.86	33.49	175.0	1×10^{18}	2.2	50.25	163.0
8×10^{15}	3.1	30.79	193.0	1×10^{18}	2.2	62.81	210.0
3×10^{15}	2.0	9.55	40.0	1×10^{18}	2.2	87.93	258.0
3×10^{15}	2.1	26.82	66.0				

Table 5: Experimental hardening according to the size and concentration of solute clusters

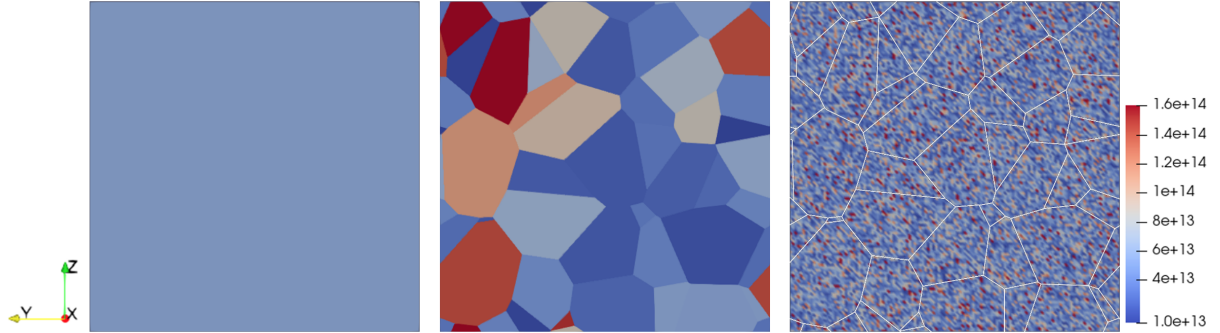


Figure 12: Initial dislocation densities fields: homogeneous (left), homogeneous per phase (center) and heterogeneous (right)

331 but different from one phase to another,

- 332 3. a heterogeneous distribution, where each voxel has a different initial dislocation density, regardless of
 333 the phase in which it is located.

334 Except for the case of a uniform distribution, the value of the initial dislocation density is a random variable
 335 and, in order to be able to compare the results obtained for these three distributions, its mean is the same for
 336 the three distributions and equal to $\mu_{init} = \rho_{init}^{(s)}$. Moreover, the standard deviation of this random variable
 337 is fixed to $\sigma_{init} = 5\mu_{init}$. The values of the initial dislocation densities are randomly drawn according to a
 338 probability distribution law (18) and (19) of the log-normal type. The choice of this law was determined by
 339 three requirements dictated by physical requirements: drawn values should be positive, the maximum value
 340 of initial dislocation densities should be close to the average value $\rho_{init}^{(s)}$ and the range of values between the
 341 maximal one and its half should be large enough.

342 The probability density for a log-normal law is given by

$$p(x, \mu_{log}, \sigma_{log}) = \frac{1}{x\sigma_{log}\sqrt{2\pi}} \exp\left(-\frac{(\ln(x) - \mu_{log})^2}{2\sigma_{log}^2}\right), \quad (18)$$

343 where the parameters μ_{log} and σ_{log} are related to the mean μ_{init} and standard deviation σ_{init} by

$$\mu_{log} = \ln(\mu_{init}) - \frac{1}{2} \ln\left(\frac{\sigma_{init}^2}{\mu_{init}^2} + 1\right) \quad \text{and} \quad \sigma_{log} = \sqrt{\ln\left(\frac{\sigma_{init}^2}{\mu_{init}^2} + 1\right)}. \quad (19)$$

344 The values of the initial dislocation densities are obtained using a random variable with uniform distribution.
 345 The three initial dislocation densities fields obtained by this procedure are presented in Figure 12 for a specific
 346 cross section.

347 The macroscopic response and the evolution of the total dislocation density obtained for each distribution
 348 of the initial dislocation densities are presented in Figure 13 for three temperatures, -100°C, 25°C and 200°C,
 349 considering the same parameters than previously. The total dislocation density is defined as

$$\bar{\rho} = \sum_{r=1}^{216} \sum_{s=1}^{12} c^{(r)} \bar{\rho}^{(r,s)} \quad (20)$$

350 where $c^{(r)}$ represents the volume fraction of the phase r . The initial value of $\bar{\rho}$ is denoted by $\bar{\rho}_{init}$. For the
 351 macroscopic response, very small differences are observed between the three distribution configurations over
 352 the strain range studied and for the three temperatures considered. At -100°C, the macroscopic responses
 353 are superposed, while at 25°C and 200°C, small differences are observed at the beginning of the viscoplastic
 354 domain between the homogeneous distribution and the two others. Nevertheless these differences tend to

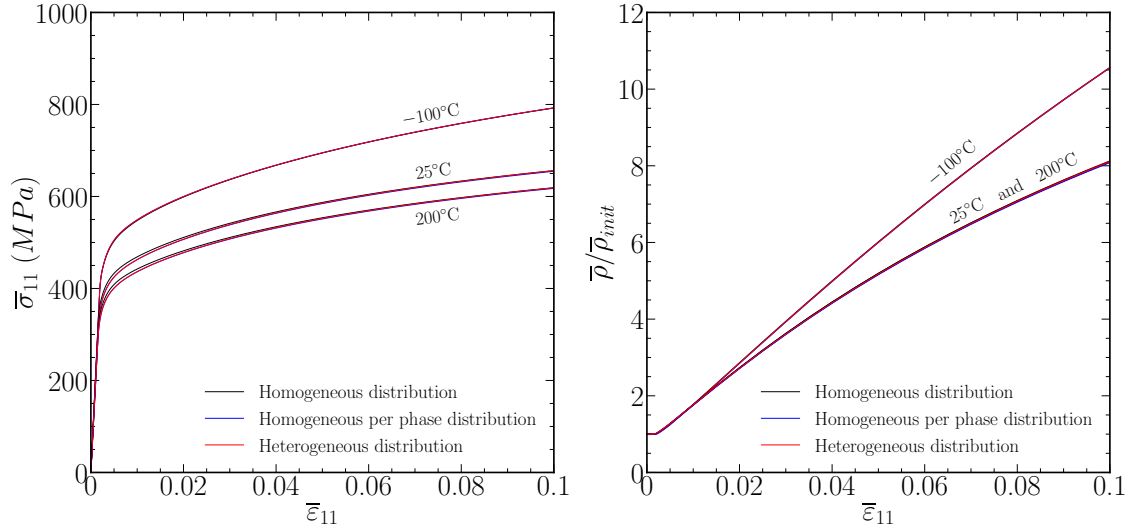


Figure 13: Macroscopic response (a) and total dislocation density, normalized by its initial value (b), for three distributions of the initial dislocation densities and for three temperatures, -100°C, 25°C and 200°C

355 reduce as the macroscopic strain increase. Concerning the evolution of the total dislocation density, it seems
 356 that the distribution of the initial dislocation densities has almost no effect on this macroscopic variable.
 357 The results for 25°C and 200°C are superimposed and this is probably due to the fact that the annihilation
 358 distance y as given by (10) no longer depends on the temperature if this one is greater than 25°C. The
 359 temperature level has a notable effect on the evolution of the total dislocation density with respect to the
 360 macroscopic strain; at low temperatures (-100°C) this evolution is less non linear and more rapidly increasing
 361 than at high temperatures (25°C and 200°C). This could be explained by the increasing of the annihilation
 362 distance (10) with the temperature which leads a diminution of the dislocation densities rates (8).

363 The effects of the initial dislocation densities are observed by analysing the Von Mises equivalent vis-
 364 coplastic strain and the maximum principal stress value, which are respectively defined by

$$\varepsilon_{vp}^{eq} = \sqrt{\frac{2}{3} \boldsymbol{\varepsilon}_{vp}^d : \boldsymbol{\varepsilon}_{vp}^d}, \quad \text{and} \quad \sigma_p^{max} = \max(\sigma_1, \sigma_2, \sigma_3), \quad (21)$$

365 where $\boldsymbol{\varepsilon}_{vp}^d$ represents the deviatoric part of the viscoplastic strain tensor and σ_i , $i = 1, 2, 3$ are the principal
 366 stresses. The local fields retained for this analysis are obtained for two effective strain values in the loading
 367 direction: $\bar{\varepsilon}_{11} = 0.004$ (which corresponds to $\bar{\varepsilon}_{vp11} = 0.002$, *i.e.* the value considered for the determination
 368 of the conventional yield stress) and $\bar{\varepsilon}_{11} = 0.1$. The first value of the macroscopic strain corresponds to the
 369 situation where the macroscopic response (Figure 13) presents the most significant difference between the
 370 three distributions considered, whereas for the second value this difference is completely smeared out.

371 Figure 14 presents the equivalent viscoplastic strain fields obtained for a uniform distribution, at $\bar{\varepsilon}_{11} =$
 372 0.004 for three resolutions, 57^3 , 125^3 and 250^3 voxels. Deformation bands can be seen in the grains circled
 373 in red, but this aspect is theoretically impossible for the case of a homogeneous distribution because the
 374 considered crystal plasticity law is not supposed to induce localizations. Furthermore, the width and number
 375 of bands evolve with the resolution, which means that this problem clearly corresponds to an artifact of
 376 the FFT method. In fact, it is here the non-respect of the grain boundaries geometry (seen as staircases)
 377 which favours the appearance of non-physical deformation bands. The work of [34] focuses on this problem
 378 and shows that the appearance of strain bands is greatly reduced by using a non regular Fourier grid, in
 379 order to correctly match the grain boundaries geometry. This aspect is therefore a prospect of this work.
 380 However, in the analysis presented hereafter the values of the local fields have no particular meaning, the
 381 analysis being purely qualitative.

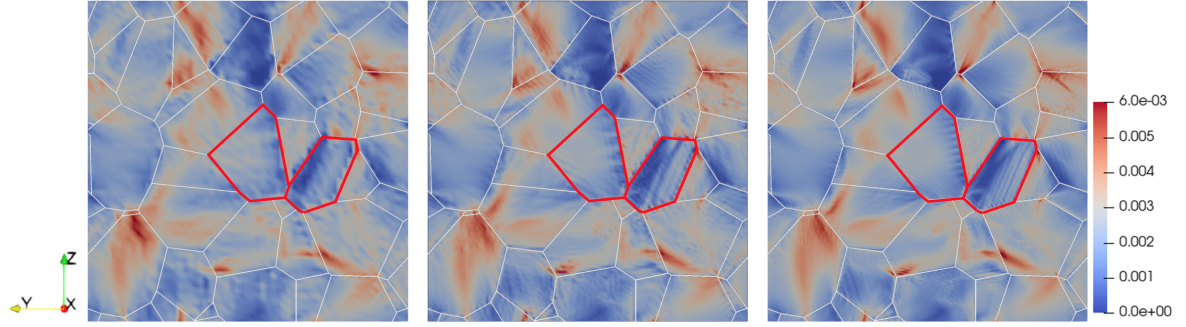


Figure 14: Von Mises equivalent viscoplastic strain fields (homogeneous distribution at $\bar{\varepsilon}_{11} = 0.004$) for three resolutions: 57^3 (left), 125^3 (center) and 250^3 (right) voxels

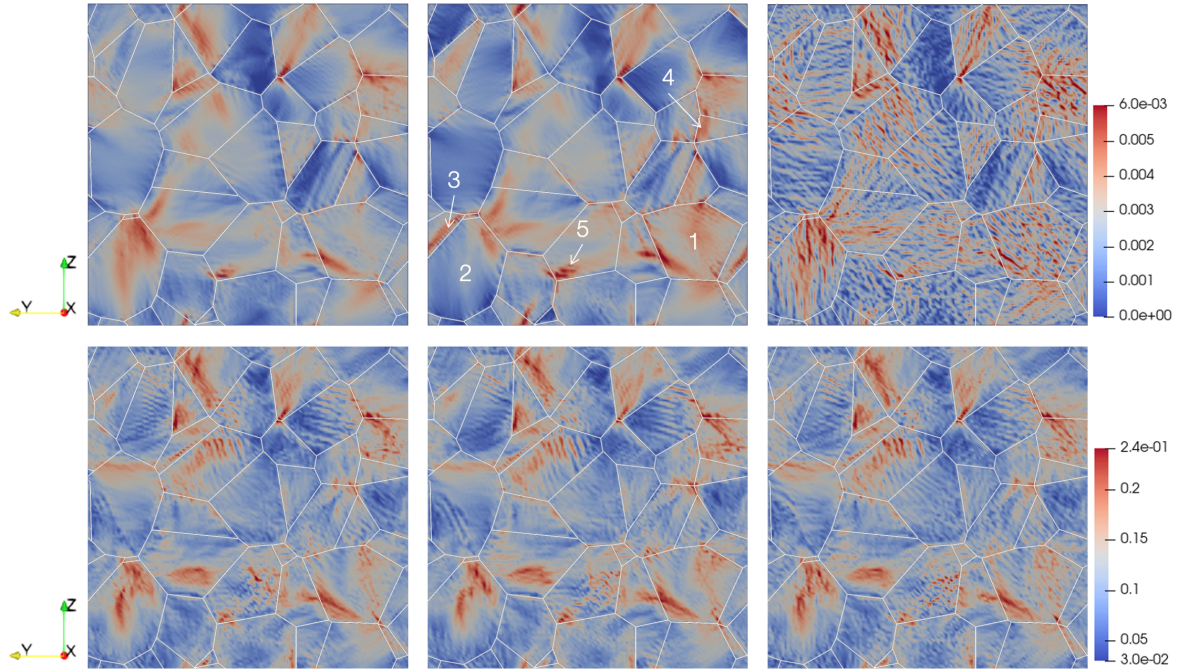


Figure 15: Von Mises equivalent viscoplastic strain fields: at $\bar{\varepsilon}_{11} = 0.004$ (up) and $\bar{\varepsilon}_{11} = 0.1$ (down)

382 Figures 15 and 16 present respectively the Von Mises equivalent viscoplastic strain field and the maximum
 383 principal stress field, for the three distributions: homogeneous (left), homogeneous per phase (center) and
 384 heterogeneous (right). At $\bar{\varepsilon}_{11} = 0.004$, three distinct field profiles are clearly identified, both for the equiva-
 385 lent viscoplastic strain and for the maximum principal stress value. Comparing the equivalent viscoplastic
 386 strain maps, between the homogeneous and homogeneous per phase distributions a strong correlation is
 387 observed between the level of the initial dislocation densities of the grains and the overall viscoplastic strain
 388 of the grains. For instance, for the grains denoted (1) and (2) on the Figure 15 the initial dislocation density
 389 is lower (for grain (1)) or higher (for grain (2)) than the mean value (affected to all grains in the case of an
 390 homogeneous distribution) and the overall viscoplastic strain is higher in grain (1) or lower in the grain (2)
 391 than the corresponding values obtained for the same grains in the case of an homogeneous distribution. Also,
 392 in the case of the homogeneous per phase distribution, notable strain localization are observed at the grain
 393 boundaries (3), (4) or at triple points (5). When comparing the maps corresponding to the homogeneous
 394 and heterogeneous distributions, the main differences are observed for the fields profiles, inside each grain,

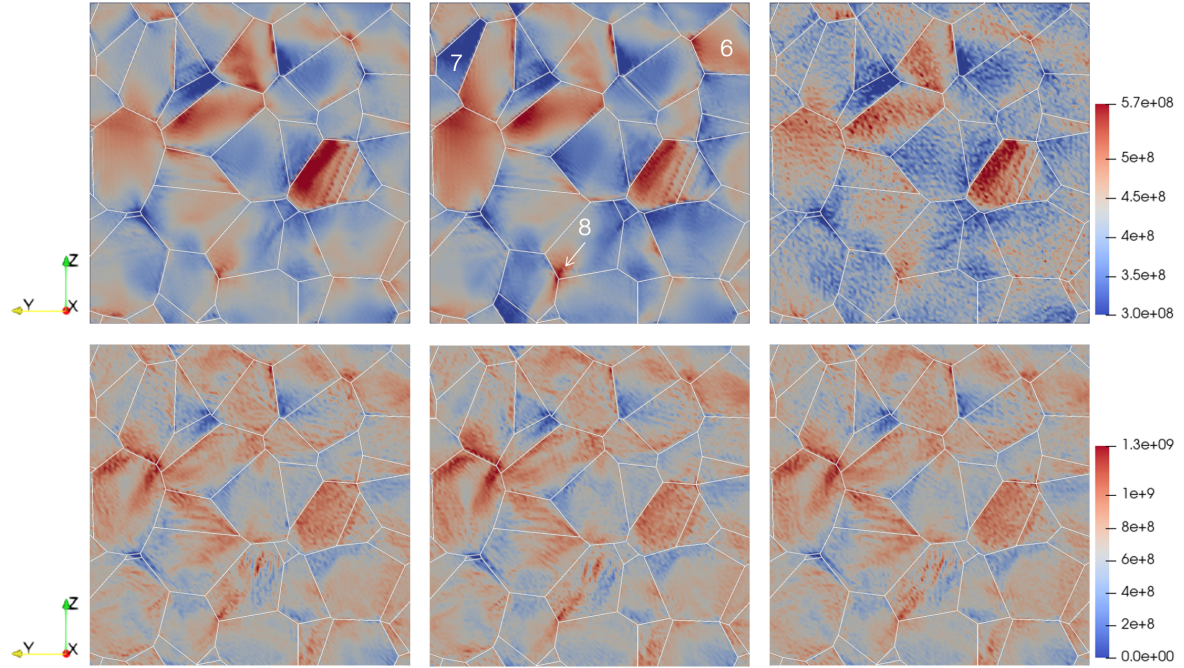


Figure 16: Maximum principal stress value fields: at $\bar{\varepsilon}_{11} = 0.004$ (up) and $\bar{\varepsilon}_{11} = 0.1$ (down)

395 due to the significant difference in initial dislocation densities from one voxel to the other nearby ones for the
 396 heterogeneous distribution. Similar conclusions can be drawn for the maximum principal stress value. The
 397 major differences between homogeneous and heterogeneous distributions are observed in the field profiles
 398 within each grain. In contrast, between homogeneous and homogeneous per phase distributions, higher (6)
 399 or lower (7) overall grain viscoplastic strain can be observed, similarly for stress concentrations (8).

400 Deep in the plastic range the observed differences between the local fields corresponding to different initial
 401 dislocation densities distributions tend to gradually fade away as the loading evolves during the simulation,
 402 to finally converge towards a common configuration. In particular, at $\bar{\varepsilon}_{11} = 0.1$, the local fields present
 403 similar profiles for the two results of interest, whatever the type of initial dislocation densities distribution
 404 considered.

405 As explained in the previous section, the local values of the fields could be not very accurate, but as
 406 shown on the Figure 11 the average value per phase of the Von Mises equivalent viscoplastic strain has an
 407 asymptotic behavior when the resolution increases. Therefore it is pertinent to compare these mean values
 408 for the three types of the initial dislocation densities distributions. The results are reported in Figure 17.
 409 In these figures, we select the first 50 phases which present the maximum difference value observed between
 410 the three distributions at $\bar{\varepsilon}_{11} = 0.004$ and the average values per phase are ordered (on the x-axis) in a
 411 decreasing manner with respect to this difference value. These results show, as previously, that the impact
 412 of the distribution of initial dislocation densities for a low strain ($\bar{\varepsilon}_{11} = 0.004$) is more pronounced than for a
 413 high strain ($\bar{\varepsilon}_{11} = 0.1$). Furthermore, these results also highlight that the homogeneous and heterogeneous
 414 distributions give very closed values for the average value per phase compared to analogous result for the
 415 homogeneous per phase distribution. This could be the consequence of a statistical effect. Each grain
 416 contains sufficiently voxels such way that the mean value of the initial dislocation density in each grain is
 417 close to the mean value of the same variable on the whole domain, so close to the value of the uniform
 418 distribution.

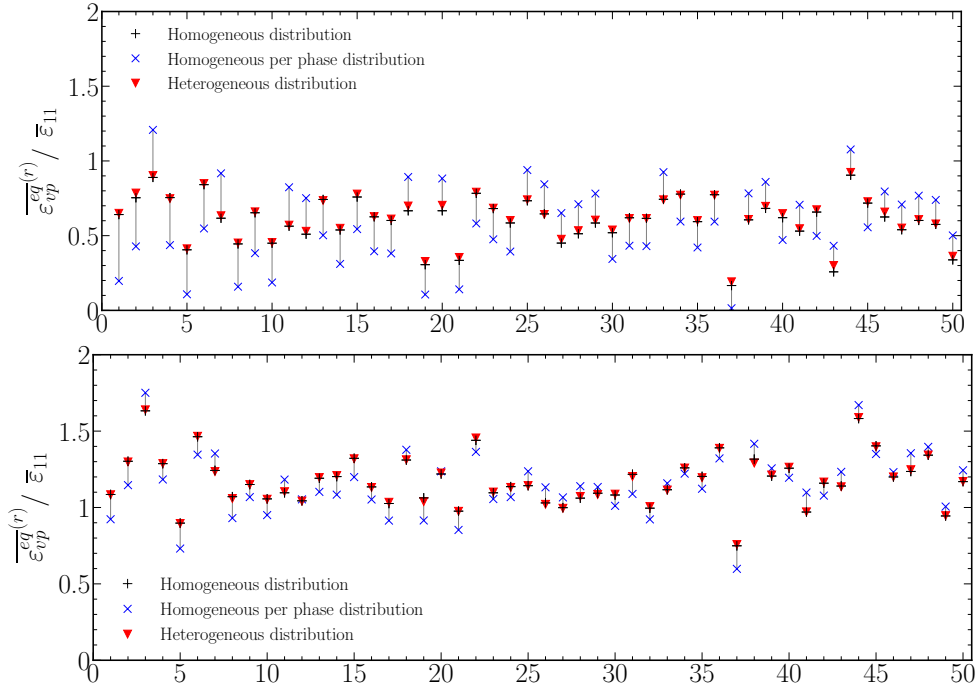


Figure 17: Average value per phase of the Von Mises equivalent viscoplastic strain: at $\bar{\epsilon}_{11} = 0.004$ (up) and $\bar{\epsilon}_{11} = 0.1$ (down)

419 5. Conclusion

420 A multi-scale model has been proposed by combining a crystal plasticity law for irradiated RPV steels
421 and numerical full-field simulations on polycrystals based on Fast Fourier Transforms. Comparisons between
422 numerical and experimental results have been performed on four types of macroscopic results in order to show
423 the relevance of the crystal plasticity law. First, the macroscopic tensile curves are accurately reproduced
424 by the numerical simulations, for a temperature range from -100°C to 200°C and for three fluences. Second,
425 the strain rate sensitivity induced by a fast variation in imposed macroscopic strain rate shows a good
426 agreement with the experimental results for a temperature range from -200°C to 100°C and for two strain-
427 rate variations $5 \times 10^{-3} \text{ s}^{-1} / 5 \times 10^{-4} \text{ s}^{-1}$ and $5 \times 10^{-4} \text{ s}^{-1} / 5 \times 10^{-5} \text{ s}^{-1}$. Third, the evolution of
428 the yield stress is generally better reproduced for low and high strain rates ($4 \times 10^{-4} \text{ s}^{-1}$ and 17.6 s^{-1})
429 than for a very high strain rate (4000 s^{-1}). Finally, the irradiation-induced hardening is well reproduced by
430 numerical simulations, over a wide range of fluences and fluxes. In these simulations, all input parameters are
431 within typical values of grain size, dislocation densities and solute cluster size and density, characteristic of
432 a irradiated low alloy RPV steels. The main advantage of this physically-based model is that when the yield
433 stresses before and after irradiation are known at a given temperature and strain rate, the model can predict
434 the yield stress at any temperature and strain rate. In addition, intragranular stress and strain fields are
435 also investigated in the case of heterogeneous distribution of initial dislocation densities. The results led to
436 differences in local fields between the three distributions at the beginning of the viscoplastic domain, which
437 tend to reduce and basically converge towards a common configuration deep in the viscoplastic domain.
438 However, the presence of non-physical strain bands are observed representing an artifact of the FFT method
439 and more precisely concerning the discretization process which not respect the grain boundaries geometry.
440 Finally, the macroscopic response and the evolution of the total dislocation density seem to be very weakly
441 influenced by the heterogeneity of dislocation density.

442 Acknowledgments

443 The work was funded by the Institute of Fusion and Instrumentation Sciences in Nuclear Environments
444 (ISFIN) and by the Institut de Radioprotection et de Sûreté Nucléaire (IRSN). Additional funds from the
445 Universidad Nacional de La Plata (UNLP) were received by M.I.I. through grant I281/2024. The authors
446 gratefully acknowledge Hervé Moulinec for his assistance in using CraFT and useful discussions about FFT
447 methods.

448 Data availability

449 This study has no part providing observations or experimentation data. All experimental results used
450 in order to validate research findings presented in this article are public data, available from cited research
451 publications and owned by their respective authors.

452 References

- 453 [1] G. Monnet, Analytical flow equation for irradiated low-alloy steels established by multiscale modeling, *Journal of Nuclear*
454 *Materials* 586 (2023) 154647.
- 455 [2] J.-P. Mathieu, Analyse et modélisation micromécanique du comportement et de la rupture fragile de l'acier 16MND5:
456 prise en compte des hétérogénéités microstructurales, Ph.D. thesis (2006).
- 457 [3] E. Bouyne, H. Flower, T. Lindley, A. Pineau, Use of EBSD technique to examine microstructure and cracking in a bainitic
458 steel, *Scripta Materialia* (1998) 295–300.
- 459 [4] G. Monnet, L. Vincent, L. Gélébart, Multiscale modeling of crystal plasticity in reactor pressure vessel steels: Prediction
460 of irradiation hardening, *Journal of Nuclear Materials* 514 (2019) 128–138.
- 461 [5] G. Monnet, L. Vincent, B. Devincere, Dislocation-dynamics based crystal plasticity law for the low- and high-temperature
462 deformation regimes of bcc crystal, *Acta Materialia* 61 (16) (2013) 6178–6190.
- 463 [6] L. Chaix, M. Gărăjeu, P.-G. Vincent, G. Monnet, M. I. Idiart, Homogenized descriptions for the elastoplastic response of
464 polycrystalline solids with complex hardening laws: Application to neutron-irradiated bainitic steels, *European Journal*
465 *of Mechanics - A/Solids* 105 (2024) 105258.
- 466 [7] H. Moulinec, P. Suquet, A fast numerical method for computing the linear and nonlinear properties of composites, *C. R.*
467 *Acad. Sc. Paris II* 318 (1994) 1417–1423.
- 468 [8] M. Schneider, A review of nonlinear FFT-based computational homogenization methods, *Acta Mech* 232 (2021) 2051–2100.
- 469 [9] A. Prakash, R. Lebensohn, Simulation of micromechanical behavior of polycrystals: Finite elements versus fast Fourier
470 transforms, *Modelling Simul. Mater. Sci. Eng* (2009) 64010–16.
- 471 [10] S. El Shawish, P.-G. Vincent, H. Moulinec, L. Cizelj, L. Gélébart, Full-field polycrystal plasticity simulations of neutron-
472 irradiated austenitic stainless steel: A comparison between FE and FFT-based approaches, *Journal of Nuclear Materials*
473 529 (2020) 151927.
- 474 [11] R. Lebensohn, N-site modeling of a 3d viscoplastic polycrystal using Fast Fourier Transform, *Acta Materialia* 49 (2001)
475 2723–2737.
- 476 [12] J. Segurado, R. Lebensohn, J. Llorca, Computational homogenization of polycrystals, *Adv. Appl. Mech.* 51 (2018) 1–114.
- 477 [13] J. Michel, H. Moulinec, P. Suquet, A computational method based on augmented lagrangians and Fast Fourier Transforms
478 for composites with high contrast, *Computer Modeling in Engineering & Sciences* 1 (2) (2000) 79–88.
- 479 [14] D. Eyre, G. Milton, A fast numerical scheme for computing the response of composites using grid refinement, *The European*
480 *Physical Journal Applied Physics* 6 (1999) 41–47.
- 481 [15] V. Monchiet, G. Bonnet, A polarization-based FFT iterative scheme for computing the effective properties of elastic
482 composites with arbitrary contrast, *Int. J. Numer. Meth. Engng* 89 (2012) 1419–1436.
- 483 [16] H. Moulinec, F. Silva, Comparison of three accelerated FFT-based schemes for computing the mechanical response of
484 composite materials, *International Journal for Numerical Methods in Engineering* 97 (13) (2014) 960–985.
- 485 [17] A. M. P. Brozzo, G. Buzzichelli, M. Mirabile, Microstructure and cleavage resistance of low-carbon bainitic steels, *Metal*
486 *Science* 11 (1977) 123–130.
- 487 [18] F. Kocks, H. Mecking, Physics and phenomenology of strain hardening: The fcc case, *Progress in Materials Science* 48
488 (2003) 171–273. doi:10.1016/S0079-6425(02)00003-8.
- 489 [19] CRAFT, Composite Response and Fourier Transforms (free software).
490 URL <https://lma-software-craft.cnrs.fr>
- 491 [20] P. Suquet, A simplified method for the prediction of homogenized elastic properties of composites with a periodic structure,
492 *C. R. Acad. Sc. Paris, II* 311 (1990) 769–774.
- 493 [21] H. Moulinec, P. Suquet, A numerical method for computing the overall response of nonlinear composites with complex
494 microstructure, *Computer Methods in Applied Mechanics and Engineering* 157 (1) (1998) 69–94.
- 495 [22] L. Joëssel, P.-G. Vincent, M. Gărăjeu, M. I. Idiart, Viscoplasticity of voided cubic crystals under hydrostatic loading,
496 *International Journal of Solids and Structures* 147 (2018) 156 – 165.

- 497 [23] P.-G. Vincent, H. Moulinec, L. Joëssel, M. I. Idiart, M. Gărăjeu, Porous polycrystal plasticity modeling of neutron-
498 irradiated austenitic stainless steels, *Journal of Nuclear Materials* 542 (2020) 152463.
- 499 [24] C. Bellis, P. Suquet, Geometric variational principles for computational homogenization, *Journal of Elasticity* 137 (2019)
500 119–149.
- 501 [25] K. Wojtacki, P.-G. Vincent, P. Suquet, H. Moulinec, G. Boittin, A micromechanical model for the secondary creep of
502 elasto-viscoplastic porous materials with two rate-sensitivity exponents: Application to a mixed oxide fuel, *International*
503 *Journal of Solids and Structures* 184 (2020) 99–113.
- 504 [26] G. Boittin, P.-G. Vincent, H. Moulinec, M. Gărăjeu, Numerical simulations and modeling of the effective plastic flow surface
505 of a biporous material with pressurized intergranular voids, *Computer Methods in Applied Mechanics and Engineering*
506 323 (2017) 174–201.
- 507 [27] R. Lebensohn, M. Idiart, P. Ponte Castañeda, P.-G. Vincent, Dilatational viscoplasticity of polycrystalline solids with
508 intergranular cavities, *Phil. Mag.* 91 (2011) 3038–3067.
- 509 [28] Y. Changqing, E. T. Chung, Convergence of trigonometric and finite-difference discretization schemes for FFT-based
510 computational micromechanics, *BIT Numerical Mathematics* 63 (1) (2023) 11.
- 511 [29] C. Ji, Y. Cui, Y. Li, N. Ghoniem, A concurrent irradiation-mechanics multiscale coupling model, *Journal of the Mechanics*
512 *and Physics of Solids* 167 (2022) 105005.
- 513 [30] B. Tanguy, J. Besson, R. Piques, A. Pineau, Ductile to brittle transition of an a508 steel characterized by Charpy impact
514 test: Part i: experimental results, *Engineering Fracture Mechanics* 72 (1) (2005) 49–72.
- 515 [31] P. B. Wells, T. Yamamoto, B. Miller, T. Milot, J. Cole, Y. Wu, G. R. Odette, Evolution of manganese–nickel–silicon-
516 dominated phases in highly irradiated reactor pressure vessel steels, *Acta Materialia* 80 (2014) 205–219.
- 517 [32] J. Hure, C. Vaille, P. Wident, D. Moinereau, C. Landron, S. Chapuliot, C. Benhamou, B. Tanguy, Warm prestress effect
518 on highly irradiated reactor pressure vessel steel, *Journal of Nuclear Materials* 464 (2015) 281–293.
- 519 [33] C. Robertson, K. Obrtlík, B. Marini, Dislocation structures in 16mnd5 pressure vessel steel strained in uniaxial tension
520 at different temperatures from -196°C up to 25°C , *Journal of Nuclear Materials* 366 (2007) 58–69.
- 521 [34] M. Zecevic, R. Lebensohn, Recent advances in fft-based methods for polycrystalline materials, 2024.